

In situ small-angle X-ray scattering reveals strong condensation of DNA origami during silicification

Martina F. Ober¹, Anna Baptist², Lea Wassermann², Amelie Heuer-Jungemann^{2,*}, and Bert Nickel^{1,*}

¹ Faculty of Physics and CeNS, Ludwig-Maximilians-Universität München, Geschwister-Scholl-Platz 1, 80539 Munich, Germany

² Max Planck Institute of Biochemistry and Center for Nanoscience (CeNS), Ludwig-Maximilians-Universität München, Am Klopferspitz 18, 82152 Martinsried, Germany

Corresponding authors: *heuer-jungemann@biochem.mpg.de, nickel@lmu.de

Abstract *The silicification of DNA origami structures increases their mechanical and thermal stability and provides chemical protection. So far, it is unclear how silicification affects the internal structure of the DNA origami and whether the whole DNA framework is embedded or if silica just forms an outer shell. By using in situ small-angle X-ray scattering (SAXS), we show that the net-cationic silica precursor TMAPS induces substantial condensation of the DNA origami, which is further enhanced by the addition of TEOS at early reaction times to an almost 10 % size reduction. We identify the SAXS Porod invariant as a reliable, model-free parameter for the evaluation of the amount of silica formation at a given time. Contrast matching of the DNA double helix Lorentzian peak reveals that silica growth also occurs on the inner surfaces of the origami. The less polar silica forming within the origami structure, replacing more than 40 % of the internal hydration water causes a hydrophobic effect: origami condensation. In the maximally condensed state, thermal stabilization of the origami up to 60 °C could be observed. If the reaction is driven beyond this point, the overall size of the silicified origami increases again due to more and more silica deposition on the DNA origami. DNA origami objects with flat surfaces show a strong tendency towards aggregation during silicification, presumably driven by the very same entropic forces causing condensation. Our studies provide novel insights into the silicification reaction and hints for the formulation of optimized reaction protocols.*

Introduction

DNA origami¹ is a versatile bottom-up nanofabrication technique to engineer nanometer-sized objects with sub-nanometer precision and complete site-specific addressability due to the programmable self-assembly of complementary DNA strands². Potential applications of such DNA origami objects are manifold and include bio-sensing³, drug delivery, as well as various biophysical⁴ and biomedical applications^{5, 6, 7, 8, 9}. A major bottleneck of utilizing DNA origami nanostructures in biomedical applications, however, is their inherent instability in common biological buffers and cellular environments as well as their susceptibility to enzymatic degradation^{10, 11, 12}. Therefore, there is a need to increase the chemical, thermal and mechanical stability of DNA origami nanostructures in order to unravel their full potential and utilization in real-life applications.

One recently reported approach to achieve higher stability of DNA origami nanostructures is their encapsulation in a protective silica shell. Resulting structures are even stable in the absence of salt-containing buffers, at high temperatures, and in the presence of nucleases^{7, 13, 14}. We demonstrated silicification of single DNA origami nanostructures and 3D DNA origami crystals¹⁵, resulting in mechanical enforcement. This stabilization allowed us to analyse these fragile origami structures in the dry state, without suffering from structural collapse^{13, 16}. Silicified DNA origami structures are promising candidates for biomedical applications and they play a prominent role for the customized synthesis of inorganic dielectric 2D^{17, 18} and 3D nanomaterials^{7, 19, 20}.

The silicification process is a sol-gel approach based on a modified Stöber reaction^{7, 13, 14}. The reaction is initiated through the electrostatic interactions of the quaternary ammonium head group of N-trimethoxysilylpropyl-N,N,N-trimethylammonium chloride (TMAPS) and the anionic DNA phosphate backbone. Siloxane groups on TMAPS then provide co-condensation sites for tetraethyl orthosilicate (TEOS) and enable silica growth. The successful growth of silica on DNA origami nanostructures was thus far mainly evidenced through analysis of structures in the dry state via transmission electron microscopy (TEM), scanning electron microscopy (SEM), atomic force microscopy (AFM) and energy dispersive X-ray spectroscopy (EDX)^{7, 13, 14}. “Shell” thicknesses were inferred indirectly through microscopy images. However, to date it is unclear how the silicification reaction commences and whether silica grows as a “shell” around the origami, or if silica also penetrates the internal structure of the helix bundles.

In view of many possible applications of silicified-DNA origami nanostructures, especially as sculptured dielectrics, detailed understanding of the internal structure is essential in order to rationalize the protective nature of the silicification and its dielectric properties. Nevertheless, conventionally applied microscopy and spectroscopy techniques do not allow for such detailed investigation and analysis. In order to gain access to the required knowledge on the silicification process, we here use small-angle X-ray scattering (SAXS), a well-established structural tool to study DNA origami^{12, 15, 21} and silica nanocomposites at physiological conditions in solution^{22, 23}. Here, via *in situ* SAXS, we reveal and quantify a TMAPS-induced condensation of the inner double helix spacing of 24 helix bundles (24HBs) and four-layered origami bricks (4-LBs), as well as an outer shape contraction. Silica forms both on the inside and outside of the DNA origami as revealed by X-ray contrast matching. The inner order of the origami and the overall shape are well-preserved. We demonstrate that silica penetration into the origami structure is the main cause for increased thermal stability up to 60°C rather than an outer silica shell. Moreover, we observe that DNA origami with flat surfaces show increased tendency towards aggregation during silicification.

Materials and Methods

Folding and purification of DNA origami structures

Both DNA origami structures used here were designed using the CaDNAo software²⁴ (design schematics in **Figure S1-3** and **Table S1**)

24HB: The 24HB structure (design schematics in **Figure S1a** and **Figure S2**) was folded using 30 nM of DNA scaffold p8064 (tilibit nanosystems GmbH, Germany), and 100 nM of each staple oligonucleotide (Eurofins Genomics Germany GmbH and Integrated DNA Technologies, Inc., USA) in buffer containing 400 mM Tris-Acetate, 1 mM EDTA (pH = 8) and 14 mM MgCl₂. The mixture was heated to 65°C and held at this temperature for 15 min, then slowly cooled down to 4°C over a period of 15 hours. For further details see¹².

The 24HBs were concentrated and purified from excess staples by two rounds of polyethylene glycol (PEG) precipitation and re-dispersion in buffer (1x TE, 3 mM MgCl₂). In brief, the origami folding solution was mixed in a 1:1 volumetric ratio with PEG precipitation buffer (15 % w/v PEG (MW: 8000 g/mol), 500 mM NaCl, 2x TE), adjusted to a MgCl₂ concentration of 10 mM and centrifuged at 16000 rcf for 25 min. The supernatant was removed and the DNA pellet was re-suspended in 0.5 mL of 1x

TE buffer containing 11 mM MgCl₂. The PEG precipitation step was repeated after 30 min of shaking, and the purified structures were re-suspended in the final buffer (1x TE, 3 mM MgCl₂). This solution was shaken for 24 h at room temperature at 350 rpm for complete dispersion of the origami. Concentration of the purified DNA origami solution (up to 270 nM or 1.4 g/L) was verified via absorption measurements (Thermo Scientific NanoDrop 1000 Spectrophotometer). The successful folding of structures was confirmed by TEM analysis. DNA origami solutions were stored at 4°C until further use.

4-LB: The 4-LB (design schematics in **Figure S1b** and **Figure S3**) was folded using 10 nM of the scaffold p8064 (tilibit nanosystems GmbH, Germany), 100 nM of each staple oligonucleotide (Integrated DNA Technologies, Inc., USA) in buffer containing 40 mM Tris, 20 mM acetic acid, 1 mM EDTA (pH = 8) and 18 mM MgCl₂. The mixture was heated to 65°C and held at this temperature for 15 min, then slowly cooled down to 20°C over a period of 16 hours. The 4-LB origami solution was concentrated and purified from excess staples by ultrafiltration. Briefly, the folding mixture (~2 mL) was divided over 4-5 Amicon Ultra filters (0.5 mL, 100 K, Millipore, USA) and each centrifuged at 8000 rcf for 8 min. The centrifugal steps were repeated 3-5 times with fresh buffer (1xTAE, 3 mM MgCl₂) added in every step. The resulting solution (~30 µL) was re-suspended in buffer and the procedure repeated. A purified origami solution of 100 - 120 µL in total with a concentration up to 270 nM (1.4 g/L) was obtained and stored at 4°C until further use. The correct folding of the DNA origami was confirmed by TEM analysis

Silica coating

110 µL of purified 24HBs (270 nM) were mixed with 0.67 µL of TMAPS (TCI, USA) (50% in methanol) and shaken at 350 rpm for 1 min in an Eppendorf tube. 2.67 µL of TEOS (Sigma Aldrich, USA) (50% in methanol) were added to the tube, followed by shaking for another 15 min. Finally, the solution was filled into a sample cell for SAXS, which tumbles slowly (50 rpm). This way, molar ratios of (1:5:12.5) of phosphate groups:TMAPS:TEOS, were achieved, respectively.

For the 4-LB structures, the TMAPS-only containing origami solution was filled after shaking at 350rpm for 1min in an Eppendorf tube into the SAXS tumbling chamber and TEOS (50% in methanol) was added 15min later directly into the SAXS tumbling chamber.

TEM Imaging

TEM imaging was carried out using a JEM-1230 transmission electron microscope (JEOL) operating at 80 kV. For sample preparation 5 -10 μL of a solution containing DNA origami structures were deposited on glow-discharged TEM grids (formvar/carbon-coated, 300 mesh Cu; TED Pella, Inc.) for at least 1 min, depending on sample concentration. For visualization, bare origami structures were negatively stained by briefly washing the grid with 5 μL of a 2% uranyl formate (UFO) solution followed by staining with UFO for 10 - 30 s. Silicified DNA origami were not stained, but washed twice with MilliQ water.

In house SAXS experiments

Most X-ray data were recorded at an in house Mo X-ray SAXS setup described in detail elsewhere²⁵. We measured at 17.4 keV X-ray energy with an X-ray beam size of 1.0 x 1.0 mm^2 at the sample position. Sample-to-detector distance was 1 m. Data were recorded using a Dectris Pilatus 3 R 300K CMOS Detector (487 x 619 pixels of size (172 x 172) μm^2). We calibrated the sample to detector distance and the beam center position with silver behenate powder.

Synchrotron SAXS experiments

SAXS data from 24HB@SiO₂ before and after heating of the sample solution to 60 °C for 30 min were recorded at the Austrian SAXS beamline at ELETTRA synchrotron using a beam energy of 8 keV²⁶ and a beam size of 0.2 x 2.0 mm^2 . The sample solution was loaded in 1.3 mm diameter quartz glass capillaries by flow-through. A Pilatus detector from Dectris Ltd., Switzerland with 981 x 1043 pixels of size 172 x 172 μm^2 served as detector.

Results

From previous reports, it is known that DNA silicification is a slow process, taking at least several hours, often up to 7 days^{7, 13, 14}. Here we followed the silicification process via an X-ray lab source using Mo characteristic radiation²⁵. Mo X-rays induce less radiation dose compared to Cu radiation of the same intensity²⁷ allowing for long in situ SAXS experiments without risk of radiation damage to the sample. Furthermore, Mo radiation allows for larger sample lengths along the beam (10 mm vs. c.a. 1.5 mm) yielding more practical geometric constrains for SAXS sample cells. As DNA origami

objects exhibit a tendency to sediment during silicification, we constructed a special cell allowing for tumbling of the sample with ~ 1 round/s around its centre to ensure well-dispersed DNA origami solutions throughout the measurement (see supporting information **note S2** for details).

The silicification reaction was continuously analysed by SAXS measurements. These measurements are then binned in time to achieve the best signal to noise ratio. We found that a binning time of 1h was sufficiently fast to follow the silicification reaction with good X-ray statistics.

Prior to silicification, a reference measurement of the purified origami was taken. The SAXS intensity distribution for the bare 24HBs is shown in **Figure 1a**. The SAXS signal $I(q)$ exhibits three distinct intensity oscillations with dips at $q \approx 0.05 \text{ \AA}^{-1}$, $q \approx 0.09 \text{ \AA}^{-1}$, and $q \approx 0.13 \text{ \AA}^{-1}$. These dips are characteristic for the cylindrical shape of 24HBs. Modelling of the 24HB as a homogeneous cylinder¹² with radius $R_{bare} = 80.1 \pm 0.2 \text{ \AA}$ allowed matching of the SAXS intensity in this q -range. At $q \approx 0.16 \text{ \AA}^{-1}$, the SAXS intensity shows an additional, Lorentzian-shaped peak, which is not predicted by the homogeneous cylinder model. In order to reproduce this feature, the structure model was extended by the designed DNA double helix arrangement in a honeycomb lattice, as schematically depicted in **Figure S1a**. Within this established approach, the interhelical distance was found to be $a_{bare} = 26.2 \pm 0.3 \text{ \AA}$. The values for R_{bare} and a_{bare} are in good agreement with our previously reported values for this origami type¹². The full structure model is detailed in the **note S3** of the supporting information.

Next, we monitored the structural changes during silicification. X-ray measurements were taken over a period of up to 80 h. Silica growth was primed by the addition of TMAPS, and subsequently initiated by the injection of TEOS (see methods for details). To determine the time required for the silicification to reach completion, we evaluated the time dependence of the Porod invariant Q (**Figure 1b**). Briefly speaking, if the silicification reaction yields a product that scatters more intensely than the solvent, the Porod invariant Q will increase, and once the reaction stops, Q will saturate. The Porod invariant Q is a model-free measure of the total scattering contrast ($\Delta\rho$) of the overall sample solution, which was obtained here essentially by numerical integration of the SAXS intensities shown in **Figure 1a**, see **note S4** for details. For the bare 24HBs we obtained $Q_{bare}^{24HB}(t = 0h) = 0.3 \cdot 10^{-3} \text{ cm}^{-1} \text{ \AA}^{-3}$. During silicification, Q increased as a function of time. Since the electron density of amorphous silica ($\rho_{SiO_2} \approx 19 \cdot 10^{-6} \text{ \AA}^{-2}$) is

larger than the electron density of water ($\rho_{H_2O} = 9.4 \cdot 10^{-6} \text{ \AA}^{-2}$), this finding is consistent with increasing silica deposition on or in the 24HBs. The Porod invariant was observed to saturate after ~ 24 h suggesting that the reaction had already finished at this time. This is an interesting finding since this time is much shorter than reaction times reported previously¹³ where reactions took up to a week. A possible explanation could be that in these reports the silicification reaction mixture was left to react undisturbed at temperatures slightly below RT, while here during the measurement gentle tumbling was applied at RT in order to avoid sedimentation. Silicification reaction kinetics are highly influenced by movement, pH and temperature, therefore tumbling at RT may have inadvertently sped up the reaction²⁸.

Per se, the Porod invariant is not sensitive to the distribution of the silica. Therefore, we now analyse the temporal intensity changes of the Lorentzian peak (I_{Lor}), which is sensitive to the inner structure of the DNA origami. Strikingly, as can be seen in **Figure 1c**, this peak vanished shortly after the reaction started. However, after running the silicification reaction for more than 4 h, the Lorentzian peak recovered in intensity, surpassing the initial intensity level and even showing a second order peak at $q \approx 0.32 \text{ \AA}^{-1}$ (cf. **Figure 1a**). The disappearance and recovery of a diffraction peak is a phenomenon known as contrast matching. Contrast matching occurs if the scattering length between an object and its matrix equals²⁹. The scattering length densities from water, DNA, and silica are $\rho_{H_2O} = 9.4 \cdot 10^{-6} \text{ \AA}^{-2}$, $\rho_{DNA} = 13 \cdot 10^{-6} \text{ \AA}^{-2}$, and $\rho_{SiO_2} \approx 19 \cdot 10^{-6} \text{ \AA}^{-2}$, respectively. In turn, once ca. 40 % of the water volume fraction within the DNA origami voids are replaced by silica ($x_{SiO_2} = 0.375$, compare **note S5** in the supporting information), contrast matching occurs, i.e., the diffraction peak vanishes, as observed in **Figure 1c** after 4 h. With more and more water being replaced by silica, contrast inversion, i.e., recovery of the diffracted intensity occurs as validated in **Figure 1c** for later reaction times. The helix peak intensity saturated after ~ 24 h in accordance with the saturation of the Porod invariant Q, indicating completion of the silicification reaction.

Previous studies on DNA origami silicification lack information on whether silica is covering exclusively the outer surface of the DNA origami object, or penetrating the inner structure as well, embedding the individual helices^{7, 13, 14, 17, 19}. The *in situ* SAXS results presented here clearly reveal that silica does form in between the double helix arrangement of the origami structure. Since the equilibrium distance of the double helix

is a balance of attractive and repulsive forces, the question arises if this balance is distorted by the presence of silica. We can verify such changes by evaluating the origami cylinder radius (R) and the interhelical distance (a) of the 24HBs (cf. **Figure 2**). Since TMAPS binds to the DNA backbone through electrostatic interactions, condensation or expansion effects, as previously observed by us for change in ionic strength, or by osmotic effects, are possible¹².

So far it was unclear to which extent silicification changes the internal structure of a DNA origami. To disentangle potential effects of TMAPS and TEOS alone, bare 24HBs were incubated with TMAPS only, and studied for several hours. The corresponding SAXS data are shown in **Figure S5**. Both the 24HB cylinder radius (R) and interhelical distance (a) show a substantial decrease in response to interaction with TMAPS (cf. **Figure 2a, b**) after an incubation time of 4 h. After eight hours, we obtained a minimal cylinder radius of $R_{min}^{TMAPS} = 73.4 \pm 0.4 \text{ \AA}$ and an interhelical distance of $a_{min}^{TMAPS} = 25.2 \pm 0.3 \text{ \AA}$. These observations indicate that the interaction of the DNA phosphate backbone with TMAPS condenses the outer radius by $6.7 \pm 0.4 \text{ \AA}$, and the DNA-double helix spacing by $1.0 \pm 0.3 \text{ \AA}$. Such a condensation of DNA origami objects in the early steps of silicification has never been observed before. We propose that TMAPS binding to the DNA backbone causes electrostatic screening reducing the repulsion between neighbouring helices^{12, 30, 31, 32}, possibly in conjunction with water depletion effects. The initial lag of 4 h incubation time suggests that TMAPS accesses the phosphate groups by obstructed diffusion.

Interestingly, we observed this condensation effect even faster if TEOS was added immediately after TMAPS injection. During the first 4 h of silica growth, the cylinder radius decreased down to $R_{min} = 74.2 \pm 0.5 \text{ \AA}$ (cf. **Figure 2c**) and the minimal interhelical distance $a_{min}(t = 8h) = 23.8 \pm 0.2 \text{ \AA}$ could already be observed after 8 h (cf. **Figure 2d**). This accelerated condensation suggests hydrophobic effects within the origami in response to early silica formation.

A naïve comparison of the radius before (R_{bare}) and after silicification (R_{SiO_2}) would suggest that there is no silica shell on the outside of the origami at all. However, since the honeycomb lattice of 24HBs remains significantly condensed even towards the end of the reaction ($a_{SiO_2} = 24.7 \pm 0.05 \text{ \AA}$), the definition of the outer silica shell thickness requires some caution. We suggest that the difference between the cylinder radius at the end of the reaction ($R_{SiO_2} = 80.4 \pm 0.1 \text{ \AA}$) to the most condensed radius (R_{min}) is a

realistic upper limit for the silica encapsulation thickness. Here, we found $(R_{SiO_2} - R_{min}) = 6.2 \pm 0.3 \text{ \AA}$. Thus, the outer silica shell thickness is clearly in the sub-nanometer range.

Silicified DNA origami show impressive thermal stability (heating up to 1200 °C)^{13, 14, 33}. We wondered if the early condensed state of the origami with about 40 % silica infill and sub-nanometer shell shows already such enhanced temperature stability. To answer this question, we heated a DNA origami at the maximally condensed state ($R = 74.5 \pm 0.4 \text{ \AA}$) to 60 °C for 30 min. Bare 24HBs fully melt at this temperature¹². Contrastingly, the silicified structures remained intact as confirmed by SAXS and TEM analysis (cf. **Figure 3**). It appears that the 40 % silica frosting in the condensed origami state provides already substantial thermal stability.

All origami discussed so far were cylindrically shaped 24HBs. We also studied brick shaped origami during silicification and noted a great tendency towards aggregation, which is already visible by naked eye as macroscopic clouds in solution. However, in view of the entropic forces at work during silicification, this is expected since depletion forces are best known for favouring aggregation of colloids³⁴. Since the outer coating here is sub-nanometer, strongly curved cylindrical origami apparently do not possess enough contact area to develop such strong aggregates. Flat surfaces of brick-like DNA structures, however, readily form aggregates. To explore this scenario on the molecular level, we investigated the silicification of a cuboid DNA origami, i.e. the 4-LB, also designed on a honeycomb lattice.

The SAXS intensity for the 4-LBs before silicification exhibits one to two distinct oscillations with dips at $q \approx 0.07 \text{ \AA}^{-1}$ and $q \approx 0.13 \text{ \AA}^{-1}$, characteristic for the overall cuboid shape of 4-LBs, see **Figure 4a**. Additionally, a pronounced Lorentzian peak arising from the honeycomb lattice design can be observed. The thickness (A) of the 4-LB origami is small enough to be extracted with high precision from the SAXS data a cuboid model (cf. **Figure 4c**). We obtained a thickness of $A_{bare} = 89.9 \pm 0.4 \text{ \AA}$. At this stage, the brick-like 4-LB origami is well dispersed, i.e., SAXS data can be modelled without the need for a structure factor.

After initiating silicification, the Porod invariant Q saturates already after ~ 4 h, i.e., much earlier than in the case of the 24HB (cf. **Figure 4b**). The overall increase of the Q value after silicification is only about half compared to that of the 24HBs. During

silica formation the brick thickness is condensed to a minimal thickness of $A_{min}(t = 56h) = 80.3 \pm 1.3\text{\AA}$. However, we did not observe a reversal of the condensation effect. In agreement with this observation, the origami reaches the contrast matching condition, i.e., the helix-helix peak vanished, but there is no recovery. Instead, we observe an upturn of SAXS intensity at small q-values during the 4-LBs' silica growth in **Figure 4a**, which is an established fingerprint of aggregation. In some cases, this aggregation gives rise to a particle-particle stacking peak (cf. **Figure S6**). We therefore conclude that DNA origami with flat surfaces show increased tendency towards aggregation during silicification possibly due to increased entropic forces on the cuboid surface. This aggregation may even obstruct influx of further silica particles into the origami. So somewhat paradoxically, the brick particles here form rather large aggregates without reaching similar silica uptake compared to cylindrical origami. Nevertheless, the 4-LB, similar to the 24HB showed increased thermal stability after 4 h of silicification, i.e. with an ultrathin outer silica coating, suggesting that enough silica deposition occurred to preserve the brick shape (**Figure S7**).

Discussion

The Porod invariant Q turns out to be a model free indicator for the kinetics and yield associated with DNA origami silicification. Silicification of DNA origami is a rather slow process and the initial phase is characterized by a pronounced condensation upon silica incorporation. In general, silicification under similar conditions exhibits two reaction phases: Initially, TMAPS primes the silica polymerization reaction which then consumes TEOS yielding "primary silica particles", or better, short silica chains of here maybe in average 3-4 units (ratio TEOS 2.5:TMAPS 1). These primary silica particles should form within minutes, i.e., much faster than the silicification reaction kinetics observed here, which takes hours. We therefore suggest that the silicification reaction of the DNA origami here is driven by phase two of the general silicification reaction; aggregation of primary silica particles and their condensation into silica networks^{28, 35, 36}. This scenario implies diffusion of the primary particles (silica chains) into the DNA origami and subsequent electrostatic binding of cationic TMAPS-TEOS precursors to anionic DNA. Binding of these less polar chains to the internal surfaces of DNA helices gives rise to hydrophobic effects, such as initial condensation of all of the origami structures studied. Binding to the outer surfaces favors strong aggregation of brick-

shaped origami, even for ultrathin shells.

Conclusions

Using *in situ* SAXS we were able to show that a strong condensation of DNA origami nanostructures occurs during silicification. Silica deposition is not limited to the outside of the origami, but also occurs within the individual helix bundles. Interestingly, cuboidal DNA origami structures showed strong signs of aggregation during silicification and an overall decreased level of silica deposition compared to cylindrical DNA origami structures. Silica “shells” observed for both origami shapes used here are in the sub-nanometer regime, yet provide sufficient stability for shape retention at high temperatures over an extended period of time. We expect that these insights into the molecular arrangements during synthesis are key to the development of enhanced silicification protocols of DNA origami needed to fabricate sculptured dielectrics. One key requirement is to prevent aggregation of planar structures, possibly by inclusion of some bulky, water-soluble silanes, which bind only to the outer origami surface due to steric hindrance. Another aspect is that the inner part of the origami should be more readily accessible to primary silica particles to prevent their assembly outside of the origami. For this purpose, small primary particles may be explored followed by subsequent further additions of TEOS. It is well-documented that TEOS, following full or partial hydrolysis preferentially reacts with larger silica clusters rather than with itself, which, in this case, would be provided by the partially silicified DNA origami³⁶. By following a careful step-by-step silicification approach, this could lead to a higher degree of control over silica shell thickness and overall structure stability.

Acknowledgements

We acknowledge financial support from the German Research Foundation (DFG) through SFB1032 (Nanoagents) projects A06 and A07 number 201269156; the BMBF grant no. 05K19WMA (LUCENT) and by the Bavarian State Ministry of Science, Research, and Arts grant “SolarTechnologies go Hybrid (SolTech)”. A.H-J acknowledges funding from the DFG through the Emmy Noether program (project no. 427981116). This work benefited from SasView software, originally developed by the DANSE project under NSF award DMR-0520547. We would like to thank Heinz Amenitsch for assistance in using the SAXS beamline at the synchrotron Elettra in Trieste and the CERIC-ERIC Consortium for the access to experimental facilities. Also, we would like to thank Marianne Braun for help with TEM imaging.

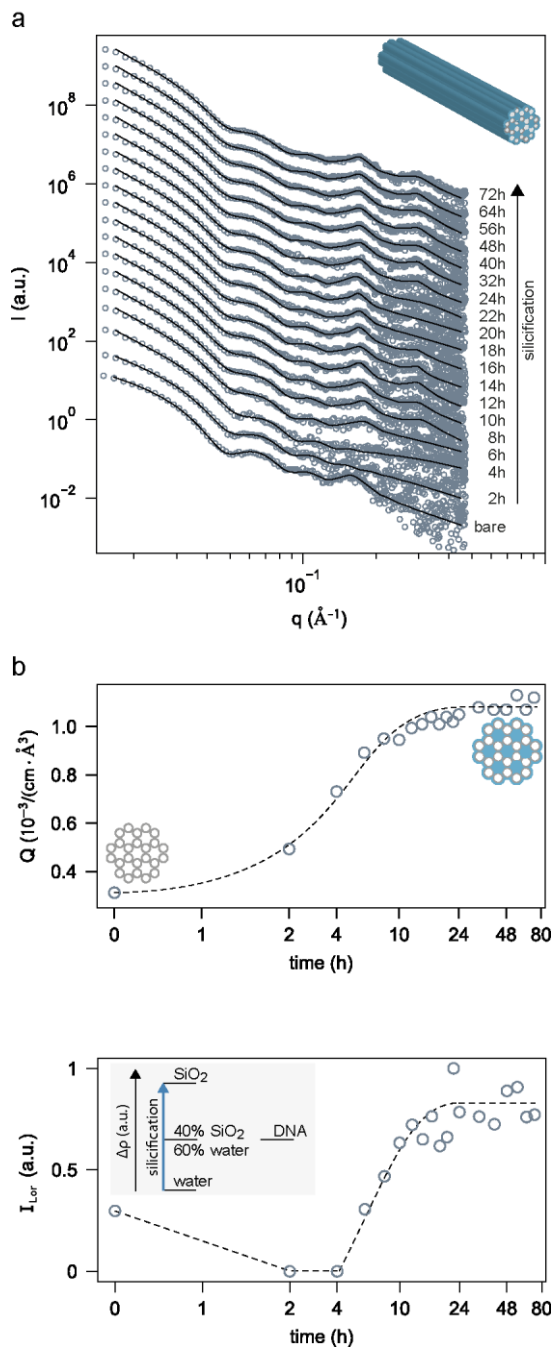


Figure 1 In situ silicification of 24HBs while tumbling with constant speed (50rpm) monitored by SAXS. SAXS data is recorded for bare 24HB and during silicification (a). The data is shown together with the best fits of a cylinder model together with Lorentzian peaks accounting for the inner honeycomb lattice arrangement. Data is scaled for clarity. Model-free Porod invariant Q (b) as a measure of the overall scattering contrast and normalized interhelical peak intensities I_{Lor} (c) are extracted from the SAXS data shown in (a) as function of silica growth time. 24HB shape with honeycomb lattice structure is shown in the inset. Dashed line serves as guide to the eye.

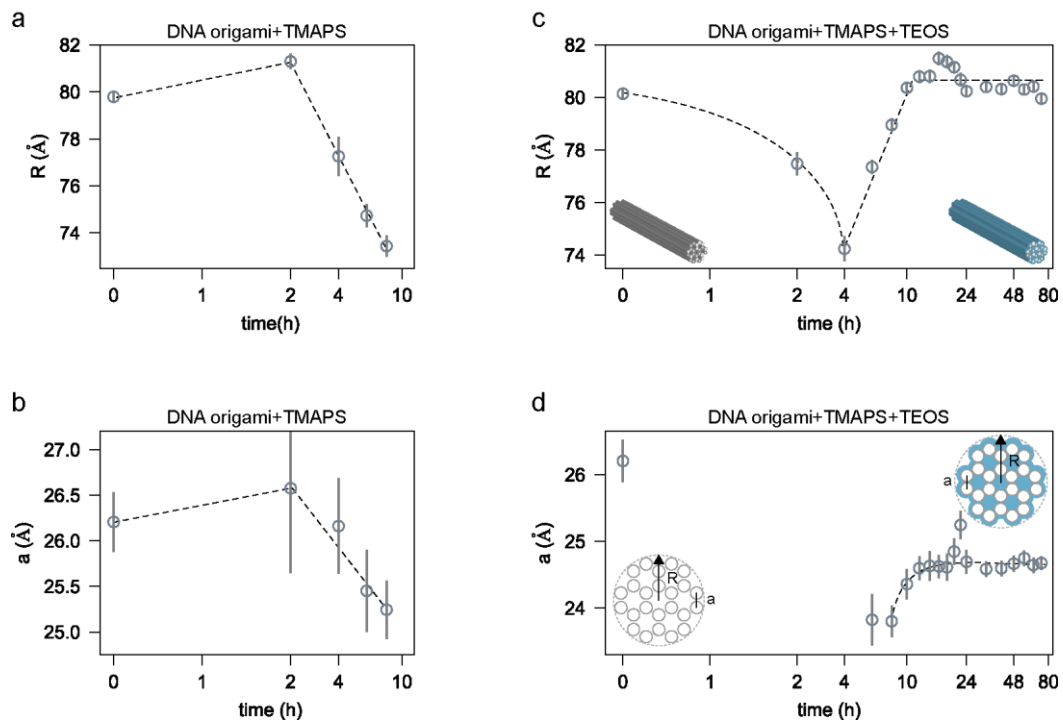


Figure 2 Radii of the overall cylinder-shaped 24HBs and interhelical distance extracted from **Figure S3** and **Figure 1a** as a function of TMAPS incubation time (a,b) and silica growth induced by TMAPS and TEOS (c,d). Dashed lines serve as guide to the eye. Schematic of the 24HB honeycomb lattice structure are shown as insets.

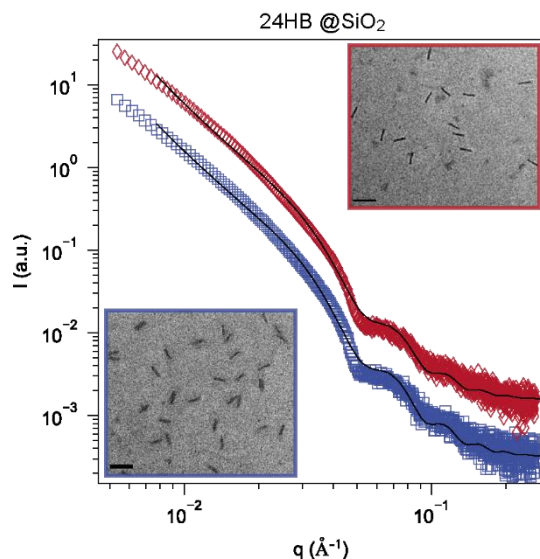


Figure 3 Temperature stability of extremely condensed silicified 24HBs verified by SAXS and TEM. SAXS intensities of 24HBs@SiO₂ ($R_{SiO_2} = 74.5 \pm 0.4 \text{\AA}$) measured at room temperature (blue squares) and after heating the structures to 60 °C for 30 min (red diamonds) and TEM micrographs of 24HB @SiO₂ at room temperature (blue frame) and after heating to 60°C for 30 min (red frame) are shown in the insets. Scale bars: 200 nm.

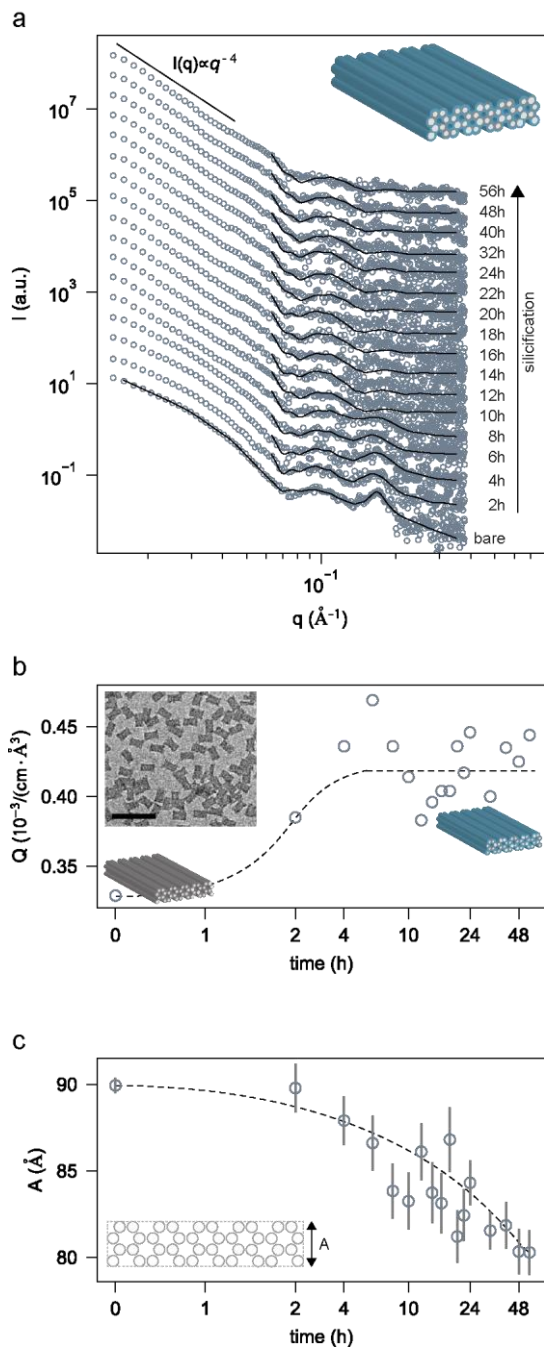


Figure 4 SAXS intensities of bare 4-LBs and during silicification together with the best fit of a cuboid model and Lorentzian peaks accounting for the honeycomb lattice structure. Data is scaled for clarity. b. Silica growth time dependence of the model-free Porod invariant Q extracted from (a) and a TEM micrograph of 4-LB @SiO₂. Scale bars: 200 nm. b. Heights of the overall cuboid shaped 4-LB as function of silica growth time. Schematic 4-LB cuboid shape with honeycomb lattice structure and front view are shown in the insets. Dashed lines serve as guide to the eye.

References

1. Rothemund PWK. Folding DNA to create nanoscale shapes and patterns. *Nature* 2006, **440**(7082): 297-302.
2. Seeman NC, Sleiman HF. DNA nanotechnology. *Nature Reviews Materials* 2018, **3**(1): 17068.
3. Ochmann SE, Vietz C, Trofymchuk K, Acuna GP, Lalkens B, Tinnefeld P. Optical Nanoantenna for Single Molecule-Based Detection of Zika Virus Nucleic Acids without Molecular Multiplication. *Analytical Chemistry* 2017, **89**(23): 13000-13007.
4. Nickels PC, Wünsch B, Holzmeister P, Bae W, Kneer LM, Grohmann D, *et al.* Molecular force spectroscopy with a DNA origami-based nanoscopic force clamp. *Science* 2016, **354**(6310): 305-307.
5. Hu Q, Li H, Wang L, Gu H, Fan C. DNA Nanotechnology-Enabled Drug Delivery Systems. *Chemical Reviews* 2019, **119**(10): 6459-6506.
6. He L, Mu J, Gang O, Chen X. Rationally Programming Nanomaterials with DNA for Biomedical Applications. *Advanced Science* 2021, **8**(8): 2003775.
7. Liu X, Zhang F, Jing X, Pan M, Liu P, Li W, *et al.* Complex silica composite nanomaterials templated with DNA origami. *Nature* 2018, **559**(7715): 593-598.
8. Berger RML, Weck JM, Kempe SM, Hill O, Liedl T, Rädler JO, *et al.* Nanoscale FasL Organization on DNA Origami to Decipher Apoptosis Signal Activation in Cells. *Small* 2021, **17**(26): 2101678.
9. Ijäs H, Shen B, Heuer-Jungemann A, Keller A, Kostianen Mauri A, Liedl T, *et al.* Unraveling the interaction between doxorubicin and DNA origami nanostructures for customizable chemotherapeutic drug release. *Nucleic Acids Research* 2021, **49**(6): 3048-3062.
10. Perrault SD, Shih WM. Virus-Inspired Membrane Encapsulation of DNA Nanostructures To Achieve In Vivo Stability. *ACS Nano* 2014, **8**(5): 5132-5140.
11. Paunescu D, Puddu M, Soellner JOB, Stoessel PR, Grass RN. Reversible DNA encapsulation in silica to produce ROS-resistant and heat-resistant synthetic DNA 'fossils'. *Nature Protocols* 2013, **8**(12): 2440-2448.
12. Fischer S, Hartl C, Frank K, Radler JO, Liedl T, Nickel B. Shape and Interhelical Spacing of DNA Origami Nanostructures Studied by Small-Angle X-ray Scattering. *Nano Lett* 2016, **16**(7): 4282-4287.
13. Nguyen L, Döblinger M, Liedl T, Heuer-Jungemann A. DNA-Origami-Templated Silica Growth by Sol-Gel Chemistry. *Angewandte Chemie International Edition* 2019, **58**(3): 912-916.
14. Nguyen M-K, Nguyen VH, Natarajan AK, Huang Y, Ryssy J, Shen B, *et al.* Ultrathin Silica Coating of DNA Origami Nanostructures. *Chemistry of Materials* 2020, **32**(15): 6657-6665.
15. Zhang T, Hartl C, Frank K, Heuer-Jungemann A, Fischer S, Nickels PC, *et al.* 3D DNA Origami Crystals. *Adv Mater* 2018: e1800273.
16. Wang Y, Dai L, Ding Z, Ji M, Liu J, Xing H, *et al.* DNA origami single crystals with Wulff shapes. *Nature Communications* 2021, **12**(1): 3011.
17. Shang Y, Li N, Liu S, Wang L, Wang Z-G, Zhang Z, *et al.* Site-Specific Synthesis of Silica Nanostructures on DNA Origami Templates. *Advanced Materials* 2020, **32**(21): 2000294.

18. Zhao Y, Zhang C, Yang L, Xu X, Xu R, Ma Q, *et al.* Programmable and Site-Specific Patterning on DNA Origami Templates with Heterogeneous Condensation of Silver and Silica. *Small* 2021: 2103877.
19. Jing X, Zhang F, Pan M, Dai X, Li J, Wang L, *et al.* Solidifying framework nucleic acids with silica. *Nature Protocols* 2019, **14**(8): 2416-2436.
20. Michelson A, Zhang H, Xiang S, Gang O. Engineered Silicon Carbide Three-Dimensional Frameworks through DNA-Prescribed Assembly. *Nano Letters* 2021, **21**(4): 1863-1870.
21. Hartl C, Frank K, Amenitsch H, Fischer S, Liedl T, Nickel B. Position Accuracy of Gold Nanoparticles on DNA Origami Structures Studied with Small-Angle X-ray Scattering. *Nano Letters* 2018, **18**(4): 2609-2615.
22. Balmer JA, Mykhaylyk OO, Armes SP, Fairclough JPA, Ryan AJ, Gummel J, *et al.* Time-Resolved Small-Angle X-ray Scattering Studies of Polymer-Silica Nanocomposite Particles: Initial Formation and Subsequent Silica Redistribution. *Journal of the American Chemical Society* 2011, **133**(4): 826-837.
23. Han H, Li L, Wang W, Tian Y, Wang Y, Wang J, *et al.* Core-Shell-Corona Silica Hybrid Nanoparticles Templated by Spherical Polyelectrolyte Brushes: A Study by Small Angle X-ray Scattering. *Langmuir* 2017, **33**(38): 9857-9865.
24. Douglas SM, Dietz H, Liedl T, Högberg B, Graf F, Shih WM. Self-assembly of DNA into nanoscale three-dimensional shapes. *Nature* 2009, **459**(7245): 414-418.
25. Bruetzel LK, Fischer S, Salditt A, Sedlak SM, Nickel B, Lipfert J. A Mo-anode-based in-house source for small-angle X-ray scattering measurements of biological macromolecules. *Review of Scientific Instruments* 2016, **87**(2): 025103.
26. Amenitsch H, Bernstorff S, Laggner P. High-flux beamline for small-angle x-ray scattering at ELETTRA. *Review of Scientific Instruments* 1995, **66**(2): 1624-1626.
27. Ober MF, Müller-Deku A, Baptist A, Amenitsch H, Thorn-Seshold O, Nickel B. SAXS measurements of azobenzene lipid vesicles reveal buffer-dependent photoswitching and quantitative Z-> E isomerisation by X-rays. *arXiv preprint arXiv:211112570* 2021.
28. Yi Z, Dumée LF, Garvey CJ, Feng C, She F, Rookes JE, *et al.* A New Insight into Growth Mechanism and Kinetics of Mesoporous Silica Nanoparticles by in Situ Small Angle X-ray Scattering. *Langmuir* 2015, **31**(30): 8478-8487.
29. Heller W. Small-angle neutron scattering and contrast variation: a powerful combination for studying biological structures. *Acta Crystallographica Section D* 2010, **66**(11): 1213-1217.
30. Qiu X, Kwok LW, Park HY, Lamb JS, Andresen K, Pollack L. Measuring Inter-DNA Potentials in Solution. *Physical Review Letters* 2006, **96**(13): 138101.
31. Roodhuizen JAL, Hendriks PJTM, Hilbers PAJ, de Greef TFA, Markvoort AJ. Counterion-Dependent Mechanisms of DNA Origami Nanostructure Stabilization Revealed by Atomistic Molecular Simulation. *ACS Nano* 2019, **13**(9): 10798-10809.
32. Ponnuswamy N, Bastings MMC, Nathwani B, Ryu JH, Chou LYT, Vinther M, *et al.* Oligolysine-based coating protects DNA nanostructures from low-salt denaturation and nuclease degradation. *Nature Communications* 2017, **8**(1): 15654.
33. Majewski PW, Michelson A, Cordeiro MAL, Tian C, Ma C, Kisslinger K, *et al.* Resilient three-dimensional ordered architectures assembled from nanoparticles by DNA. *Science Advances* 2021, **7**(12): eabf0617.

34. Lin K-h, Crocker JC, Prasad V, Schofield A, Weitz DA, Lubensky TC, *et al.* Entropically Driven Colloidal Crystallization on Patterned Surfaces. *Physical Review Letters* 2000, **85**(8): 1770-1773.
35. Keefer KD, Schaefer DW. Growth of Fractally Rough Colloids. *Physical Review Letters* 1986, **56**(22): 2376-2379.
36. Han Y, Lu Z, Teng Z, Liang J, Guo Z, Wang D, *et al.* Unraveling the Growth Mechanism of Silica Particles in the Stöber Method: In Situ Seeded Growth Model. *Langmuir* 2017, **33**(23): 5879-5890.